



**HAL**  
open science

# Large temperature difference heat dominated flow simulations using a pressure-based lattice Boltzmann method with mass correction

Guanxiong Wang, Lincheng Xu, Eric Serre, Pierre Sagaut

► **To cite this version:**

Guanxiong Wang, Lincheng Xu, Eric Serre, Pierre Sagaut. Large temperature difference heat dominated flow simulations using a pressure-based lattice Boltzmann method with mass correction. *Physics of Fluids*, 2021, 33 (11), pp.116107. 10.1063/5.0073178 . hal-03438869

**HAL Id: hal-03438869**

**<https://hal.science/hal-03438869v1>**

Submitted on 22 Nov 2021

**HAL** is a multi-disciplinary open access archive for the deposit and dissemination of scientific research documents, whether they are published or not. The documents may come from teaching and research institutions in France or abroad, or from public or private research centers.

L'archive ouverte pluridisciplinaire **HAL**, est destinée au dépôt et à la diffusion de documents scientifiques de niveau recherche, publiés ou non, émanant des établissements d'enseignement et de recherche français ou étrangers, des laboratoires publics ou privés.

1 **Large temperature difference heat dominated flow simulations using a**  
2 **pressure-based Lattice Boltzmann method with mass correction**

3 Guanxiong WANG (王冠雄),<sup>1</sup> Lincheng XU (徐林程),<sup>1</sup> Eric SERRE,<sup>1</sup> and Pierre  
4 SAGAUT<sup>1</sup>

5 *Aix-Marseille University, CNRS, Centrale Marseille, M2P2, Marseille,*  
6 *France*

7 (\*Electronic mail: lincheng.XU@univ-amu.fr.)

8 (Dated: 22 October 2021)

9 The paper addresses the simulation of heat dominated compressible flows in a closed cav-  
10 ity using a pressure-based lattice Boltzmann (LB) method in which the thermal effects are  
11 modelled by applying a pressure-featured zero-order moment of the distribution functions.  
12 A focus is made on the conservation of mass at boundary nodes, which is a challenging  
13 issue significantly complicated by the density-decoupled zero-order moment here. The  
14 mass leakage at boundary nodes is mathematically quantified, which enables an efficient  
15 local mass correction scheme. The performance of this solver is assessed by simulating  
16 buoyancy-driven flows in a closed differentially heated cavity with large temperature dif-  
17 ferences (non-Boussinesq) at Rayleigh numbers ranging from  $10^3$  to  $10^7$ . The simulations  
18 show that mass leakage at solid walls in such configurations is a critical issue to obtain  
19 reliable solutions, and that it eventually leads to simulations overflow when the cavity is  
20 inclined. The proposed mass correction scheme is however shown to be effective to control  
21 mass leakage and get accurate solutions. Thus, associated with the proposed mass conser-  
22 vation scheme, the pressure-based LB method becomes reliable to study natural convection  
23 dominated flows at large temperature differences in closed geometries with mesh aligned  
24 boundaries or not.

## 25 I. INTRODUCTION

26 Heat-dominated fluid dynamics is prevalent in both thermal sciences and engineering applica-  
27 tions from low speed flow to high speed flow, such as the rising “thermals”<sup>25</sup> used by soaring birds,  
28 various cooling systems for electronic devices, nuclear reactors, chemical processing equipment,  
29 cooling system in automotive vehicles and in turbomachinery. Despite that great progress has been  
30 made in understanding the relevant physics in different backgrounds, heat-dominated flow at high  
31 Raleigh numbers (e.g.  $> 10^7$ ) still remains challenging for both experiments and numerical sim-  
32 ulations. Mainly, the challenges can be attributed to the complex physics caused by the potential  
33 large temperature gradients<sup>1,2</sup>.

34 As a typical heat-transfer scene, the natural thermal fluid convection driven by buoyancy force  
35 due to density and temperature variations has been intensively investigated both experimentally<sup>3,4</sup>  
36 and numerically<sup>5–11</sup>. In contrast to the numerical simulations, the thermal fluid experiments are  
37 more reliable, but are also much more expensive and difficult to manipulate fluid parameters and  
38 boundary conditions<sup>3,12</sup>. However, many of the existed numerical schemes proposed to solve  
39 heat-dominated flows were mainly limited to solutions with small temperature variations where  
40 the Boussinesq approximation is reasonable to apply<sup>8,10</sup>. Numerical methods adequate for ther-  
41 mal fluid dynamics with large temperature variations are of high demand, and are under faster  
42 developing<sup>13,14</sup>. Especially, different from the traditional CFD methodologies, the relatively new  
43 lattice Boltzmann (LB) method using Cartesian grid is promising to provide efficient simulations  
44 for heat-dominated flows due to its advantages of simple parallel implementation, full compatibil-  
45 ity with complex geometries, and high computational efficiency for unsteady flow<sup>15</sup>.

46 To date, the LB method has not only achieved a reputation in the weakly compressible isother-  
47 mal flow region<sup>15</sup>, but also been extended to thermal compressible flow. First, under the low Mach  
48 number limit ( $Ma < 0.2$ ), several pressure-based LB algorithms<sup>16–20</sup> have been proposed with the  
49 energy equation either solved by another LB process (the well-known DDF method)<sup>18,21</sup> or by  
50 the conventional finite difference (FD) method (known as the hybrid method)<sup>17,19,20,22</sup>. These low  
51  $Ma$  pressure-based LB methods have been successfully applied in different thermal flows, such as  
52 combustion<sup>19,20</sup>, thermal flow with variable fluid properties<sup>21</sup> and multi-physical flow<sup>23</sup>. Second  
53 but more importantly, improved LB methods capable of thermal flow from low  $Ma$  to high  $Ma$   
54 (e.g.  $Ma = 1$ ) have been recently proposed, including the density-based LB method improved by  
55 Feng, Sagaut, and Tao<sup>13</sup> and the pressure-based LB method developed by Farag *et al.*<sup>14,24</sup>. Both

56 of these two methods adopted the hybrid strategy solving the energy equation using conventional  
57 finite difference schemes to maintain the high computational efficiency. The main difference is  
58 that Farag’s method includes the temperature in the LB framework by modifying the zeroth order  
59 moment of the distribution functions, while Feng’s method modifies the second order moment.  
60 Comparatively, Farag’s method exhibited superior capability for supersonic flow up to  $Ma \approx 4^{24}$   
61 while Feng’s method is up to  $Ma \approx 1.5$ . Since these two method remain within the classic LB  
62 framework, they are much more simple and efficient than the multi-speed (MS)<sup>25–27</sup> approach  
63 which adopts enlarged discrete velocity set (e.g. D2Q27 and D3Q343) to restore the energy equa-  
64 tion directly. The recent commercial solver ProLB adopting Farag’s pressure-based LB method  
65 has exhibited superior capability for subsonic and supersonic flows, and is promising to model  
66 complex thermal fluid dynamics with both low  $Ma$  and relatively high  $Ma$  involved. With the goal  
67 to address with a unique solver in ProLB complex industrial flow configurations with low and high  
68  $Ma$  regions and improve the efficiency in terms of developments, support and use, we extend in  
69 this work its capability to deal with natural convection dominated flows at low speed and large  
70 temperature difference.

71 Although the above mentioned thermal LB method is theoretically able to model thermal flow,  
72 the reported validations were all based on aligned boundaries. Actually, mass conservation (or  
73 mass leakage) along non-aligned boundaries is a substantial challenge to extend the LB method  
74 to heat-dominated simulations, and this is especially true for the Farag’s pressure-based method.  
75 The mass leakage (ML) problem has been noticed and reported since a long time<sup>28–30</sup>. It has been  
76 theoretically proved very recently by Xu *et al.*<sup>31</sup> to be inevitable for general LB methods using  
77 boundary treatments of at least second-order accuracy at general boundaries. Moreover, it was  
78 pointed out<sup>31</sup> that the ML problem could be more serious for flow featuring significant compress-  
79 ible effect, which is a prominent in heat-dominated flow at high Rayleigh numbers, because fluid  
80 compressibility is a direct source of the mass leakage. For the Farag’s method, the implemen-  
81 tation of mass conservation is supposed to be significantly complicated because the redefinition  
82 of the zeroth order moment of the LB distribution functions is decoupled from the fluid density.  
83 Therefore, it is critical to identify the mass leakage and to implement mass correction to apply the  
84 Farag’s pressure-based LB method to heat-dominated flows simulations.

85 Based on the above analysis, in this paper, we focus on extending Farag’s pressure-based  
86 LB method using mass correction to simulate heat-dominated flow with aligned and non-aligned  
87 boundaries. The rest of this paper is organized as follows: Firstly fundamentals of Farag’s

88 pressure-based LB model are briefed in §II. Then the mass leakage at boundary nodes is theoreti-  
 89 cally identified in §III. Based on that, the pressure-based LB method using mass correction is used  
 90 to simulate heat dominated flow with aligned and inclined boundaries at a wide range of Rayleigh  
 91 numbers in §V. Finally, some critical conclusions are drawn in §VI.

## 92 II. FUNDAMENTALS OF FARAG'S PRESSURE-BASED LB METHOD

93 Farag's pressure-based LB method<sup>14</sup> solves the full Navier-Stokes equations with the mass and  
 94 momentum equations solved within the LB framework and the energy equation computed by using  
 95 traditional finite difference (FD) schemes. The two processes are thoroughly coupled. The fluid  
 96 density and velocity resolved in the LB process is directly used to conduct the thermal convective  
 97 behaviors in the conventional CFD process. In turn the conventionally resolved thermal variable is  
 98 directly included in the definition of the zeroth order moment of the distribution functions during  
 99 the LB collision process (see Appendix B). Details of the FD schemes solving the energy equation  
 100 is provided in Appendix C.

101 Here, we concentrate on the LB part with an emphasis on the mass conversation issue. For sake  
 102 of simplicity but without loss of generality, the classical BGK model is used to demonstrated the  
 103 basic characteristics, i.e.,

$$104 \quad f_i(t + \Delta t, \mathbf{x} + \mathbf{e}_i \Delta t) - f_i(t, \mathbf{x}) = -\frac{1}{\tau}(f_i - f_i^{eq}) + \frac{\Delta t}{2} F_i \quad (1)$$

105 where  $f_i$  is the  $i^{th}$  distribution function,  $t$  is time,  $\Delta t$  is the time step,  $\mathbf{x}$  is the Eulerian coordinate  
 106 vector of a lattice node,  $\mathbf{e}_i$  is the  $i^{th}$  discrete velocity,  $\tau$  is the relaxation parameter determined as  
 107  $\tau = 1/2 + \mu/(\rho c_s^2 \Delta t)$  with  $c_s$  being the sound speed and  $\mu$  being the fluid dynamic viscosity,  $f_i^{eq}$  is  
 108 the equilibrium part of  $f_i$ , and  $F_i$  is the  $i^{th}$  external force term according to Guo's model<sup>32</sup>. The LB  
 109 equation (1) is usually solved by directly decomposing it into a linear stream process (the left-hand  
 110 side) and a local non-linear collision process (the right-hand side).  $f_i$  is the distribution function  
 111 after the stream process, and  $f_i^{col}$  will be used to denote that after the collision process.

112 In Farag's pressure-based method, the temperature is directly included in the definition of  $f_i^{eq}$   
 113 to model thermal and compressible effects, i.e.,

$$114 \quad f_i^{eq} = \omega_i \left[ \rho \theta + \frac{e_{i\alpha}}{c_s^2} \rho u_\alpha + \frac{e_{i\alpha} e_{i\beta} - c_s^2 \delta_{\alpha\beta}}{2c_s^4} : \rho u_\alpha u_\beta + \frac{e_{i\alpha} e_{i\beta} e_{i\gamma} - c_s^2 [e_i \delta]_{\alpha\beta\gamma}}{6c_s^6} : \rho u_\alpha u_\beta u_\gamma \right] \quad (2)$$

115 where the Einstein summation convention is applied,  $\omega_i$  is the  $i^{th}$  weight factor,  $\rho$  is the fluid  
 116 density,  $\theta = T/T_{ref}$  is the normalized temperature,  $u_\alpha$  is the  $\alpha^{th}$  velocity component with  $\alpha, \beta, \gamma$

117 being coordinate indices, and  $[e_i \delta]_{\alpha\beta\gamma} = e_{i\alpha} \delta_{\beta\gamma} + e_{i\beta} \delta_{\alpha\gamma} + e_{i\gamma} \delta_{\alpha\beta}$ . Consistently, the first three  
 118 moments of the distribution functions can be expressed as

$$119 \quad \sum f_i^{col} = p/c_s^2 = \rho\theta, \quad \sum f_i e_i = \sum f_i^{col} e_i = \rho\mathbf{u}, \quad \sum f_i e_i e_i = \sum f_i^{col} e_i e_i = \rho\mathbf{u}\mathbf{u} + p\mathbf{I} \quad (3)$$

120 where  $\sum$  represents summation over the whole discrete velocity set,  $p$  is the pressure, and  $\mathbf{I}$   
 121 is the identity matrix. Noticeably, the zeroth order moment of  $f_i$  is not given above because it is  
 122 significantly complicated by the implementation of mass conservation and will be demonstrated  
 123 in the followed paragraphs.

124 As illustrated in Eq. (3), the main difference compared to the classical LB method is that the  
 125 zeroth order moment is directly related to the pressure instead of the usually used density (i.e.,  
 126  $\sum f_i^{eq} = \rho$ ). Due to this modification, on one hand the compressible Navier-Stokes momentum  
 127 equation is fully restored within the LB conception, on the other hand the summation of  $f_i$  is no  
 128 longer directly related the mass conservation, and hence the mass equation cannot directly restored  
 129 from the stream and collision processes.

130 Alternatively, the mass conservation equation is enforced in a way combining the LB and the  
 131 traditional FD conceptions. Similar to the classical LB method, the mass flux can be properly  
 132 approximated during stream process since it directly depends on the first-order moment, i.e.,

$$133 \quad \begin{aligned} \nabla(\rho\mathbf{u}) &= -\sum \frac{f_i(t+\Delta t, \mathbf{x}) - f_i^{col}(t, \mathbf{x})}{\Delta t} = -\sum \frac{f_i(t, \mathbf{x} - \mathbf{e}_i \Delta t) - f_i^{col}(t, \mathbf{x})}{\Delta t} \\ &= \nabla \sum \mathbf{e}_i f_i^{col}(t, \mathbf{x}) + O(\Delta t) \end{aligned} \quad (4)$$

134 Accordingly, the mass equation can be discretized as

$$135 \quad \frac{\rho(t+\Delta t, \mathbf{x}) - \rho(t, \mathbf{x})}{\Delta t} = -\nabla(\rho\mathbf{u}) + O(\Delta t) = \sum \frac{f_i(t+\Delta t, \mathbf{x}) - f_i^{col}(t, \mathbf{x})}{\Delta t} \quad (5)$$

136 It should be noticed that, to this step, the discretization scheme in Eq. (5) is still shared by  
 137 Farag's pressure-based and the classical density-based LB methods. According to the widely  
 138 applied Chapman-Enskog analysis<sup>33</sup>, this scheme is actually of second order accuracy because the  
 139 first-order error term in the left-hand side is implicitly resolved to second-order accuracy in the  
 140 stream process in the right-hand side.

141 By substituting the zeroth order moment of  $f_i^{col}$  (see (3)) into Eq. (5), the density is consistently  
 142 updated as

$$143 \quad \rho(t+\Delta t, \mathbf{x}) = \rho(t, \mathbf{x}) + \sum f_i(t+\Delta t, \mathbf{x}) - (\rho\theta)(t, \mathbf{x}) \quad (6)$$

144 Clearly, the zeroth order moment of  $f_i$  is apparently distinguished from that of  $f_i^{col}$  or  $f_i^{eq}$  by  
145 including the time derivative of  $\rho$ , which significantly complicated the relationship between the  
146 distribution functions and the mass conservation.

147 From the above description, we can conclude that by incorporating the conventionally solved  
148 temperature into the definition of the zeroth order of the LB distribution functions and applying a  
149 consistently modified implementation of mass conservation, Farag’s pressured-based LB method  
150 successfully recovers the mass and compressible momentum equations to second order accuracy.  
151 In this way, the weakly compressible limitation is removed with most of the favorable charac-  
152 teristics of the LB method maintained. However, since the physical meaning of the distribution  
153 functions is significantly complicated and cannot be solely expressed by their moments, the bound-  
154 ary treatments directly focusing on reconstructing the unknown distribution functions cannot be  
155 used within the pressure-based LB method without significant adjustment. In contrast, the ex-  
156 isting immersed boundary methods focusing on reconstructing macroscopic variables (e.g. the  
157 interpolation-based IB method implemented in ProLB) can be directly extended in the pressure-  
158 based LB method.

### 159 III. MASS LEAKAGE QUANTIFICATION

160 In this section, mass leakage (ML) within Farag’s pressure-based LB framework is measured by  
161 adopting the bounce-back (BB) conception widely used in the classic density-based LB method.  
162 The main challenge to complete this ML measurement is that the physical definition of the ze-  
163 roth order moment of the distribution functions varies during the stream and collision processes,  
164 and its expression of macroscopic variables could be rather complex for ML analysis (see §II).  
165 Whereas, the mass leakage is conceptually a non-physical mass flux through the boundaries dur-  
166 ing the convective stream process, which is mainly determined by the first-order moment of the  
167 distribution functions, e.g.  $\rho \mathbf{u} = \sum f_i \mathbf{e}_i$ . Since  $\rho \mathbf{u} = \sum f_i \mathbf{e}_i = \sum f_i^{col} \mathbf{e}_i$  is shared throughout both  
168 Farag’s method and the classic LB method, the mass leakage analysis achieved in the classic LB  
169 frame can be definitely extended to its pressure-based counterpart. In the rest of this paper, only  
170 static boundaries are considered.

171 For the classic density-based LB method, the widely accepted definition of mass leakage is the

172 net loss of distribution functions during the stream process at boundary nodes (see Fig. III), i.e.,

$$173 \quad E(\mathbf{x}) = \frac{\Delta x}{\Delta t} \sum_{\mathbf{x} + \mathbf{e}_i \Delta t \in S} \left[ f_i^{col}(\mathbf{x}) - f_{\bar{i}}^{col}(\mathbf{x} + \mathbf{e}_i \Delta t) \right] \quad (7)$$

174 where  $S$  represents the non-fluid area,  $\Delta x$  is the grid spacing, and  $\Delta t$  is the time step, and  $\mathbf{e}_i$  is  
 175 the  $i^{th}$  discrete velocity with its components taking values among 0 and  $\pm \Delta x / \Delta t$ . Actually,  $E$  in  
 176 Eq. (7) is an approximation of the local mass flux cross the boundary, i.e.,

$$177 \quad \begin{aligned} E(\mathbf{x}) &= \frac{\Delta x}{\Delta t} \sum_{\mathbf{x} + \mathbf{e}_i \Delta t \in S} \left[ f_i^{col}(\mathbf{x}) - f_{\bar{i}}^{col}(\mathbf{x} + \mathbf{e}_i \Delta t) \right] \\ &\approx \sum f_{i,w} \text{Sign}(\mathbf{e}_i \cdot \mathbf{n}) \approx \sum f_{i,w} \mathbf{e}_i \cdot \mathbf{n} = \rho \mathbf{u}_w \cdot \mathbf{n} = 0 \end{aligned} \quad (8)$$

178 where the sub-index  $w$  represents the involved wall boundary,  $\mathbf{e}_{\bar{i}} = -\mathbf{e}_i$ , and  $\mathbf{n}$  is the local  
 179 normal vector at the boundary. The relationship (8) is of first-order accuracy for aligned bound-  
 180 aries, otherwise is of zero-order accuracy<sup>31</sup>. Despite the perturbations of the approximation to  
 181 the conventional mass flux,  $E$  has been demonstrated as an effective and accurate measurement  
 182 of the mass leakage within the classic LB framework. For example, the well-known BB scheme,  
 183 directly assigning the distribution functions streaming towards non-fluid areas to those associated  
 184 with the reversed velocity directions yielding  $E = 0$  at every node, is the only known boundary  
 185 treatment satisfying the mass conversation well. In addition, Eq. (8) clearly demonstrates that  
 186 the reasonability of  $E$  in Eq. (7) stems from the first-order moment definition of  $f_i$  as mentioned  
 187 above.

188 However, Eq. (7) cannot be directly applied within Farag's pressure-based LB method in a  
 189 clean way (e.g. the classic BB scheme) due to the complicated relationship between  $f_i$  and  $\rho$ . To  
 190 avoid this complexity, it is appealing to express the ML definition in Eq. (7) from a macroscopic  
 191 viewpoint before going to the pressure-based framework. This can be achieved by including the  
 192 distribution functions streaming from the neighbouring fluid nodes and boundary nodes (see Fig.  
 193 III) into Eq. (7), i.e.,

$$194 \quad \begin{aligned} E(\mathbf{x}) &= \frac{\Delta x}{\Delta t} \left[ \sum_{\mathbf{x} + \mathbf{e}_i \Delta t \in S} f_i^{col}(\mathbf{x}) + \sum_{\mathbf{x} + \mathbf{e}_i \Delta t \in F} f_i^{col}(\mathbf{x} + \mathbf{e}_i \Delta t) \right] \\ &\quad - \frac{\Delta x}{\Delta t} \left[ \sum_{\mathbf{x} + \mathbf{e}_i \Delta t \in S} f_{\bar{i}}^{col}(\mathbf{x} + \mathbf{e}_i \Delta t) + \sum_{\mathbf{x} + \mathbf{e}_i \Delta t \in F} f_{\bar{i}}^{col}(\mathbf{x} + \mathbf{e}_i \Delta t) \right] \\ &= \frac{\Delta x}{\Delta t} [\rho^{BB}(\mathbf{x}) - \rho(\mathbf{x})] \end{aligned} \quad (9)$$



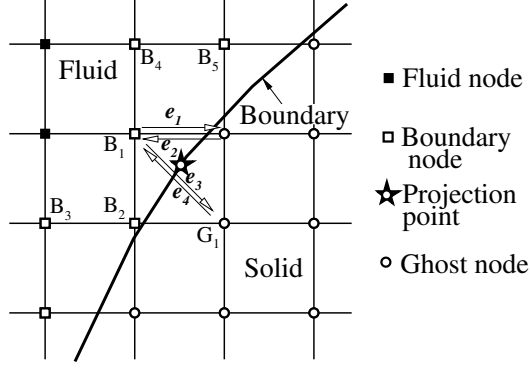


FIG. 1. Sketches of the streaming process at boundary nodes considering a D2Q9 lattice. Nodes in the solid area, e.g.  $G_1$ , are not necessary.

195 where  $F$  represents the fluid domain,  $\rho^{BB}$  is the density applying the BB strategy satisfying  
 196  $E = 0$  at every boundary node, and  $\rho$  is the density reconstructed by specific boundary treatments.  
 197 Clearly, Eq. (9) is now independent of the zero-moment definition of  $f_i$ , and thus can be used to  
 198 measure the mass leakage for both the LB methods. The remained problem is to construct  $\rho^{BB}$   
 199 properly within Farag's pressure-based LB framework.

201 Considering that the distribution functions in Eq. (9) are actually the post-stream distribution  
 202 functions at  $\mathbf{x}$ , the required  $\rho^{BB}$  can be determined by the mass conservation equation (6) as

$$\rho^{BB}(t + \Delta t, \mathbf{x}) = \rho(t, \mathbf{x}) + \left[ \sum_{\mathbf{x} + \mathbf{e}_i \Delta t \in S} f_i^{col}(t, \mathbf{x}) + \sum_{\mathbf{x} + \mathbf{e}_i \Delta t \in F} f_i^{col}(t, \mathbf{x} + \mathbf{e}_i \Delta t) \right] - \rho(t, \mathbf{x}) \theta(t, \mathbf{x}) \quad (10)$$

204 Similarly, the other distribution functions in Eq. (9) is implicitly included in  $\rho(t + \Delta t, \mathbf{x})$ .  
 205 Therefore, by substituting Eq. (10) into Eq. (9), the mass leakage within Farag's pressure-based  
 206 LB framework can be formulated as

$$E(t + \Delta t, \mathbf{x}) = \frac{\Delta x}{\Delta t} \left[ \rho(t, \mathbf{x}) + \sum_{\mathbf{x} + \mathbf{e}_i \Delta t \in S} f_i^{col}(t, \mathbf{x}) \right. \\ \left. + \sum_{\mathbf{x} + \mathbf{e}_i \Delta t \in F} f_i^{col}(t, \mathbf{x} + \mathbf{e}_i \Delta t) - \rho(t, \mathbf{x}) \theta(t, \mathbf{x}) - \rho(t + \Delta t, \mathbf{x}) \right] \quad (11)$$

208 Consequently, the local density correction can be expressed as

$$\begin{aligned}
\Delta\rho(t + \Delta t, \mathbf{x}) &= \frac{\Delta t}{\Delta x} E(t + \Delta t, \mathbf{x}) \\
&= \rho(t, \mathbf{x}) + \left[ \sum_{\mathbf{x} + \mathbf{e}_i \Delta t \in S} f_i^{col}(t, \mathbf{x}) + \sum_{\mathbf{x} + \mathbf{e}_i \Delta t \in F} f_i^{col}(t, \mathbf{x} + \mathbf{e}_i \Delta t) \right] \\
&\quad - \rho(t, \mathbf{x}) \theta(t, \mathbf{x}) - \rho(t + \Delta t, \mathbf{x})
\end{aligned} \tag{12}$$

Similar to the local mass correction methods used by Bao, Yuan, and Schaefer<sup>29</sup>, in the rest of this paper,  $\Delta\rho$  in Eq. (12) will be directly used to correct the density at boundary nodes, i.e.,  $\rho(\mathbf{x}) = \rho^{BB}$ .

#### IV. PHYSICAL CONFIGURATION AND NUMERICAL SETUP

The canonical natural convection flow in a heated square cavity is considered in this paper to assess Farag’s pressure-based LB method using mass correction in simulating heat-dominated flow. The method based on the D3Q19 model (see Appendix A) is implemented in the commercial solver ProLB with the energy equation conventionally solved (see Appendix C). The recursively regularized technique<sup>34,35</sup> is adopted to facilitate stable solutions. A cut-cell immersed boundary (IB) method is used to implement the boundary conditions<sup>36</sup> for both the LB process and the FD procedure (see Appendix D). In this IB method, the macroscopic variables (e.g. the density, velocity and temperature) at the boundary nodes are interpolated from their surrounding fluid nodes and nearest boundary points so that the equilibrium distribution functions can be reconstructed. Meanwhile, the non-equilibrium distributions are reconstructed from the derivatives of the macroscopic variables generated during the macroscopic interpolations. For the simulations conducted in this paper, uniform grid strategy is applied over the whole fluid domain (see Fig. 2).

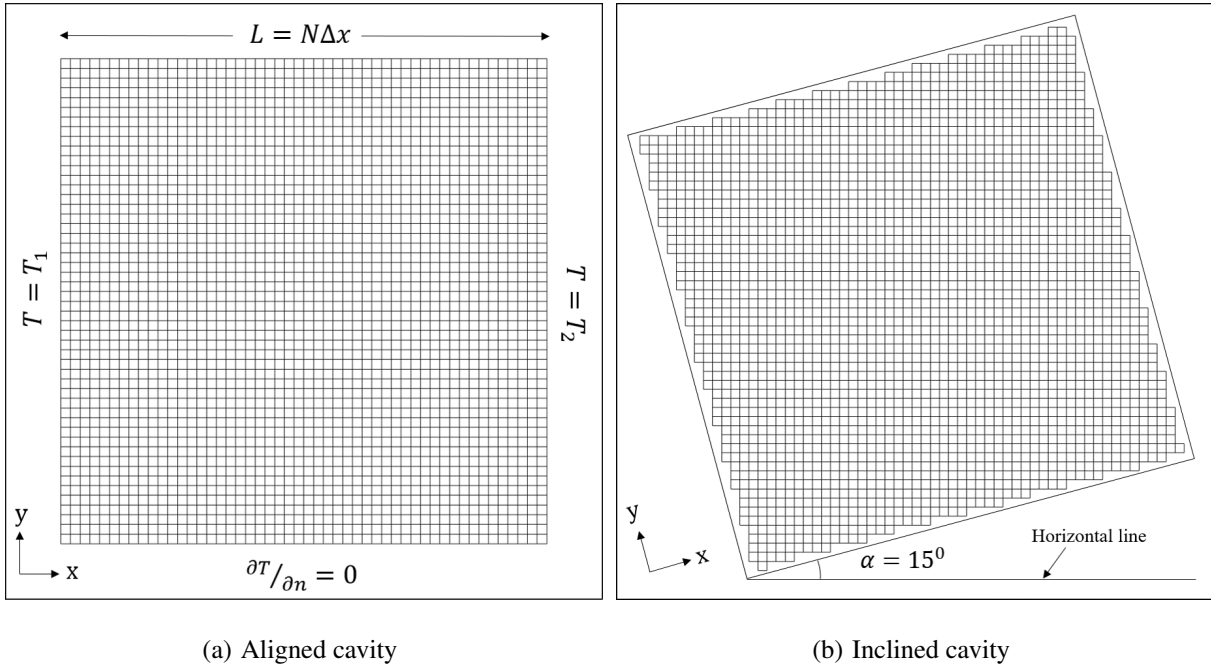
The physical configuration of the heated square cavity is shown in Fig. 2. The air modeled as a perfect gas satisfying  $P = \rho RT$  ( $R$  is the gas constant) is considered in the fluid domain. Sutherland’s law is utilized to compute the dynamic viscosity  $\mu(T) = \mu^* * (\frac{T}{T^*})^{3/2} * \frac{T^* + S}{T + S}$  with  $T^* = 273K$ ,  $S = 110.5K$ , and  $\mu^* = 1.68 * 10^{-5} kgm^{-1}s^{-1}$ . The thermal conductivity is calculated by  $\lambda(T) = \frac{\mu(T)C_p}{Pr}$  with  $C_p$  being the specific heat capacity of air and  $Pr = 0.71$ . For the wall boundaries, as shown in Fig. 2, isothermal conditions are assigned to the left and right walls with the temperature fixed at  $T_1$  and  $T_2$ , respectively, while the top and bottom walls are set to be adiabatic (i.e.,  $\partial T / \partial n = 0$ ). Meanwhile,  $\partial p / \partial n = 0$  is applied to all the boundaries, and an external gravity is imposed on the fluid. Consequently, the flow is resulted from the interaction

235 among the implied gravity, the buoyancy force caused by thermal effect, and the fluid viscosity.  
 236 Accordingly, the Rayleigh number, the ratio between the buoyancy force and viscous force, is the  
 237 main characteristic parameter, i.e.,

$$238 \quad Ra = \frac{g\rho_0^2\Delta TL^3Pr}{T_0\mu_0^2} \quad (13)$$

239 where  $g$  is the gravity acceleration,  $\rho_0, T_0 = (T_1 + T_2)/2$  and  $\mu_0$  is the reference density, mean  
 240 temperature and the fluid dynamic viscosity, respectively,  $\Delta T = T_2 - T_1$ ,  $Pr$  is the Prandt number,  
 241 and  $L$  is the length of the cavity serving as a free parameter to change the Rayleigh number.  
 242 Besides, the normalized temperature gap (i.e.,  $\varepsilon = \frac{T_1 - T_2}{T_1 + T_2}$ ), indicating the variation amplitude of  
 243 the temperature, is another important characteristic parameter for the heat-dominated flow.

244 In the concerned numerical assessment, heat-dominated flow with  $T_1 = 240K$ ,  $T_2 = 960K$  and  
 245 thus a large  $\varepsilon = 0.6$  (the Boussinesq assumption requires  $\varepsilon < 0.1$ ) is simulated over a wide range  
 246 of  $Ra$ , i.e.,  $10^3 \leq Ra \leq 10^7$ . Moreover, cavities inclined at different angles from  $0^\circ$  to  $45^\circ$  (see Fig.  
 247 2(b)) are included to verify the capability for non-aligned boundaries.



248 FIG. 2. Aligned (a) and inclined (b) heated square cavities with uniform Cartesian grid  $\Delta x/L = 0.02$ .

249  
 250 To facilitate quantitative analysis in the rest of this paper, some critical physical measurements  
 251 are introduced here. Firstly, following Vierendeels, Merci, and Dick<sup>11</sup>, the Nusselt number  $Nu$   
 252 measuring heat flux across the vertical walls as well as its averaged value  $\overline{Nu}$  is defined as:

$$253 \quad Nu(y) = \frac{L}{\lambda_0\Delta T} \lambda \frac{\partial T}{\partial x} \Big|_{wall} \quad \overline{Nu} = \frac{1}{L} \int_{y=0}^{y=L} Nu(y) dy \quad (14)$$

254 Secondly, mass leakage in the cavity simulations is measured by the overall mass loss normalized  
 255 as

$$256 \quad ML = \frac{\sum_V \rho^n - \sum_V \rho_0}{\sum_V \rho_0} \quad (15)$$

257 where  $V$  represents the whole fluid domain. In addition,  $U_{ref} = \frac{Ra^{0.5} \mu(T_0)}{\rho_0 L}$  is used as the reference  
 258 velocity<sup>11</sup> in the rest of this paper.

## 259 V. RESULTS AND DISCUSSION

260 The assessment of Farag’s pressure-based LB method using mass correction in heat-dominated  
 261 flow over  $10^3 \leq Ra \leq 10^7$  is conducted using the ProLB software in this section. Firstly, the mass  
 262 leakage as well as the caused problems are analyzed in §V A. Then, performance of the mass  
 263 correction equipped method for non-aligned boundaries is assessed in §V B. Finally, performance  
 264 of the method over the considered Rayleigh number range is assessed in §V C.

### 265 A. Mass leakage quantification and its effect on thermal simulations

266 The mass leakage in thermal simulations using Farag’s pressure-based LB method as well as  
 267 its influence on the solutions (e.g. the heat flux estimation) is investigated here.  $Ra = 10^7$  is used  
 268 in the simulations as it is supposed to be associated with the most complex thermal physics for  
 269 the considered range of Rayleigh numbers,  $10^3 \leq Ra \leq 10^7$ . Without loss of generality, the cavity  
 270 inclined at  $15^\circ$  is considered to study the effect of non-aligned boundaries. In addition, different  
 272 grid sizes (from  $N^2 = 50^2$  to  $400^2$ ) are tested to clarify its effect on the ML problems.

273 Fig. 3 shows the history of the overall ML for both aligned and inclined cavity using different  
 274 grid resolutions. As can be observed, the mass leakage accumulates with time in all the cases.  
 275 For the simulations with non-aligned boundaries, the mass leakage is so significant that all the  
 276 simulations crash in the early stage. In contrast, for the cases with aligned boundaries, the mass  
 277 leakage decreases significantly with refining grid spacing, from about -80% using  $N^2 = 50^2$  to  
 278 about 3% using  $N^2 = 400^2$  at  $U_{ref} t / L = 250$ . However, even with relatively low increasing rate, the  
 279 accumulated ML still leads to computation crash finally, e.g. this occurs at around  $U_{ref} t / L = 400$   
 280 in the case with  $N^2 = 200^2$ . The observed dependence of ML on grid spacing and boundary  
 281 orientation is consistent with the theoretical analysis of ML reported in Ref.<sup>31</sup> for general LB  
 282 methods.

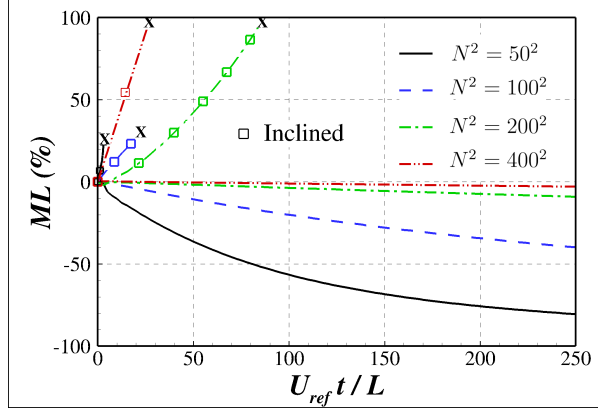
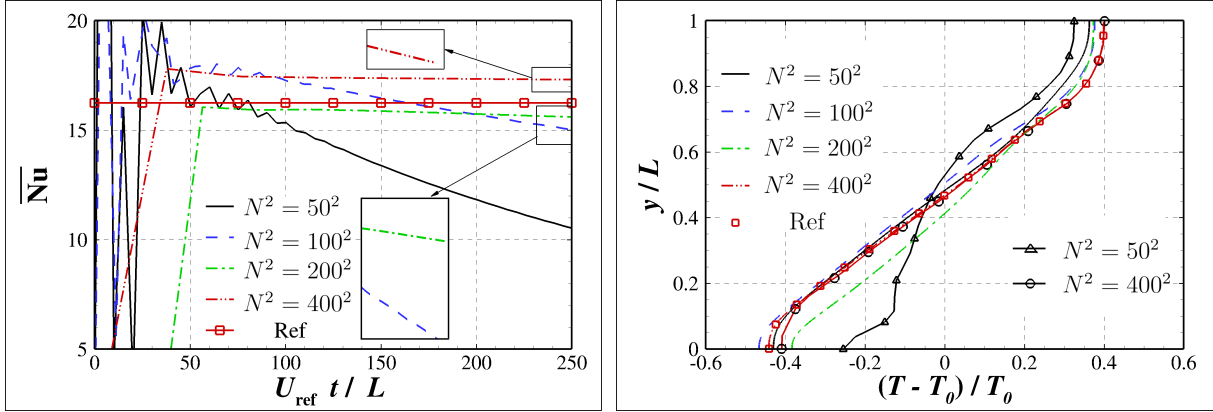


FIG. 3. Time histories of mass leakage at  $Ra = 10^7$  for aligned and inclined cavity (lines with square markers). The x markers indicate crashed computation.



(a)  $\overline{Nu}$

(b) Temperature profiles

FIG. 4. Time history of  $\overline{Nu}$  (a) and temperature profile at  $x/L = 0.5$  and  $U_{ref}t/L = 250$  (b). In (b), result from Ref.<sup>35</sup> (lines with markers) is included for comparison.

283 To clarify the influence of the observed ML on the solutions, time histories of the averaged  
 284 Nusselt number along the aligned wall in the right side and the temperature profiles at  $x/L = 0.5$   
 285 and  $U_{ref}t/L = 250$  are plotted in Fig. 4(a) and (b), respectively. As we can see, for all the  
 286 tested grid resolutions,  $\overline{Nu}$  (see Fig. 4(a)) firstly increases with time during the thermal convection  
 287 establishment, but it then decreases gradually after  $U_{ref}t/L = 250$  to the end of the simulations.  
 288 Similar to the ML displayed in Fig. 3, the decreasing rate of  $\overline{Nu}$  as well as the discrepancy of  
 289 the temperature profiles (see Fig. 4(b)) reduces with increasing  $N$ . Although these behaviours are  
 290 usually deemed as a pure grid spacing converging process (e.g. in Ref.<sup>35</sup>), the problem is actually  
 291 beyond that because of two reasons. First, the monotonic decreasing trend of  $\overline{Nu}$  is non-physical

292 since the simulations are supposed to reach a steady state featuring a constant  $\overline{Nu}$ . Second, due to  
 293 the accumulating mass leakage, the reasonable result obtained using very fine grid (e.g.  $N = 400$ )  
 294 can not be maintained with more time steps simulated. Therefore, it can be concluded that, for the  
 295 considered thermal simulation, ML is a critical challenge that refining grids could relieve it. In  
 296 addition, as shown in Fig. 4(b), the grid spacing depended discrepancy of the temperature profiles  
 297 is more obvious in the result reported in Ref.<sup>35</sup> using an improved density-based LB method,  
 298 indicating that the ML challenge might be also critical in other LB frameworks.

## 299 **B. Effectiveness of the mass correction scheme**

300 To cure the mass leakage problem observed in the last subsection, we implemented a local  
 301 mass correction (MC) method in the solver based on the theoretical analysis proposed in §III.  
 302 Effectiveness of the MC method is assessed here. First, similar to the ML analysis in §V A, the  
 303 cases with aligned boundaries considering different grid resolutions ( $50 \leq N \leq 400$ ) are analyzed.  
 304 Second, the heated cavity inclined at different angles from  $0^\circ$  to  $45^\circ$  is simulated to assess the  
 305 robustness of the mass corrected LB method. Still, the most representative  $Ra = 10^7$  is considered.

306 Before detailed physical analysis, it is pointed out that mass leakage measured by Eq. (15) in  
 307 all the considered simulations is exactly zero, indicating that the theoretical mass leakage analysis  
 308 for Farag's pressure-based LB method is accurate and reliable.

309 Fig. 5(a) and 5(b) display the time history of  $\overline{Nu}$  and the temperature profiles at  $x/L = 0.5$ ,  
 310 respectively, for the cases with aligned boundaries. As shown in Fig. 5(b), all the results with  
 311  $N$  from 50 to 400 converge well to the reference data from Ref.<sup>11</sup>, exhibiting substantially im-  
 312 provement compared to those without mass correction shown in Fig. 4(a). Consistently, all the  
 313 temperature profiles shown in Fig. 5(b) achieve excellent agreement with the reference data, which  
 314 is significantly improved from those without mass correction shown in Fig. 4(b). Clearly, the mass  
 315 correction not only improves the reliability of the simulations, but also allows using coarse grid  
 316 resolution to achieve good results thus significantly improve the computational efficiency. Be-  
 317 sides, the observed improvement using mass correction also confirms that the problems observed  
 318 in §V A is mainly caused by mass leakage.

319 Fig. 6 shows the temperature contours at  $U_{ref}t/L = 250$  for inclination angle increasing from  
 320  $0^\circ$  (aligned boundaries) to  $45^\circ$  with an increment of  $15^\circ$ . As can be seen, the solutions are almost  
 321 independent of the inclined angles. The most observable discrepancy is near the bottom wall of  $45^\circ$

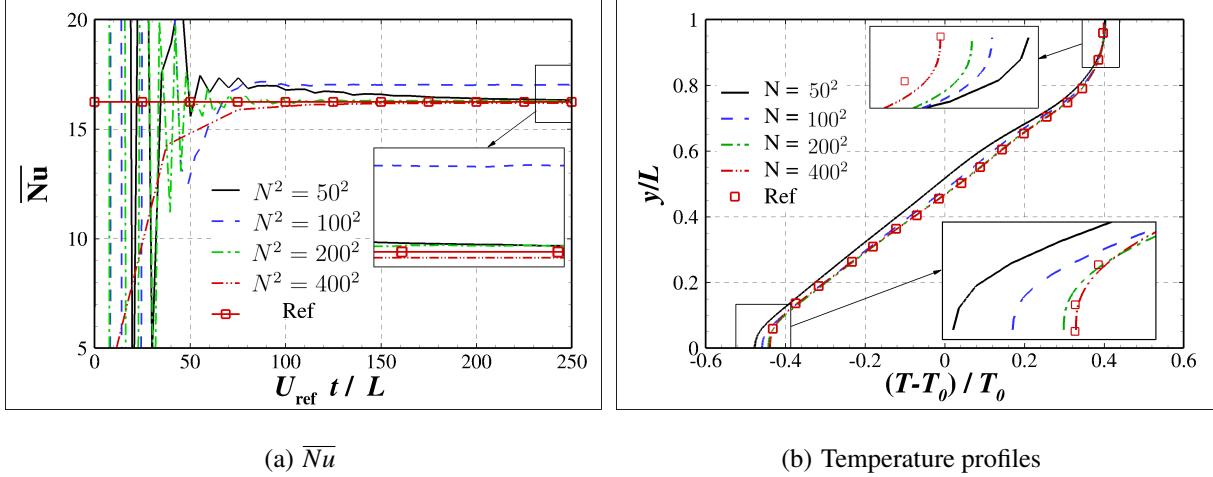


FIG. 5. Time history of  $\overline{Nu}$  (a) and temperature profile at  $x/L = 0.5$  and  $U_{ref}t/L = 250$  (b) for  $Ra = 10^7$ .

322 inclined cavity. Similar conclusion can be also drawn from the corresponding  $\overline{Nu}$  listed in Table  
 323 I. The observed discrepancy is supposed to be associated with the fact observed in Ref.<sup>31</sup> that  
 324 boundary nodes along  $45^\circ$  inclined boundaries tend to produce the most significant mass leakage,  
 325 which might introduce unfavorable coupling with the heat flux in the considered configuration.

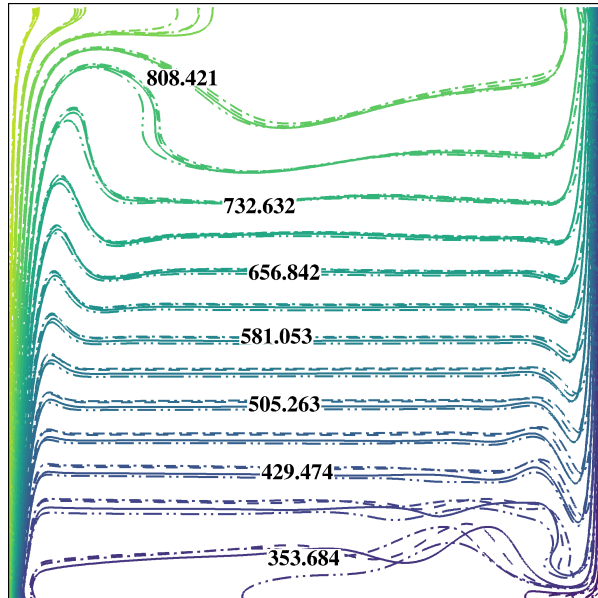


FIG. 6. Temperature contour of  $Ra=10^7$  and grid resolution  $N^2 = 400^2$  at inclined angle  $0^\circ$  (solid line),  $15^\circ$  (dashed line),  $30^\circ$  (dash dotted line) and  $45^\circ$  (dash dot dot line)

TABLE I. Average Nusselt number at different angles of inclination  $\alpha$  compared with reference Vierendeels, Merci, and Dick<sup>11</sup>

$\alpha$	0°	15°	30°	45°	Ref
$\overline{Nu}$	16.24	16.22	16.13	15.40	16.24
<b>Error (%)</b>	0.0	-0.12	-0.67	-5.17	—

### 326 C. Performance over $10^3 \leq Ra \leq 10^7$

327 The performance of Farag's pressure-based method using mass correction in heat-dominated  
 328 flow over  $10^3 \leq Ra \leq 10^7$  is assessed now. The value of  $Ra$  is changed by altering  $L$  with the other  
 329 parameters (e.g.  $T_1, T_2$ ) unchanged. The cavities are inclined at 15° to include the influence of non-  
 330 aligned boundaries. Grid convergence is performed for all the considered  $Ra$  with good results rep-  
 331 resented by Fig. 4(a) and (b) at  $Ra = 10^7$ . To facilitate consistent comparison with previous stud-  
 332 ies, results for  $Ra = 10^3, 10^4, 10^5, 10^6, 10^7$  are presented with  $N^2 = 100^2, 100^2, 200^2, 200^2, 400^2$ ,  
 333 respectively.

334 Table II display  $\overline{Nu}$  of the considered simulations. As can be seen, the heat flux increases sig-  
 335 nificantly with  $Ra$  from  $\overline{Nu} = 1.11$  at  $Ra = 10^3$  to  $\overline{Nu} = 16.22$  at  $Ra = 10^7$ , indicating a physically  
 336 increasing thermal convection. The increasingly dominating thermal convection is corroborated by  
 337 the increasing Mach number shown in Fig. 7 where the maximum  $Ma$  increases from  $7.5 \times 10^{-5}$   
 338 at  $Ra = 10^3$  to  $2 \times 10^{-4}$  at  $Ra = 10^7$  (the reference sound speed corresponding to  $T_0 = 600K$  is  
 339 unchanged). Meanwhile, for the considered  $10^3 \leq Ra \leq 10^7$ , the present results achieve good  
 340 agreement (relative difference within 1%) with the data reported in Ref.<sup>11</sup>, and considerably out-  
 341 perform those reported by Feng *et al.* applying an improved density-based LB method using very  
 342 fine grids ( $N = 800$ ) in an aligned cavity. In addition, profiles of temperature and velocity along  
 343 different lines are shown in Fig. 8(a)-(c). As can be observed, the above observed increasing trend  
 344 of  $\overline{Nu}$  is consistent with the increasing temperature gradient near the wall shown in Fig. 8(b).  
 345 Meanwhile, the present results agree well with the reference data reported in Ref.<sup>11</sup>, indicating  
 346 that the heat-dominated flows are well reproduced by the solver.



TABLE II.  $\overline{Nu}$  at inclined angle  $15^\circ$  in the range of  $10^3 \leq Ra \leq 10^7$ . Data reported by Feng *et al.* in Ref.<sup>35</sup> is included for comparison, and those in Ref.<sup>11</sup> is used as the reference.

Ra	Present	Feng <i>et al.</i> <sup>35</sup>	Ref. <sup>11</sup>	Error (%) Present VS Feng <i>et al.</i> <sup>35</sup>
$10^3$	1.11	—	1.11	0.0 vs —
$10^4$	2.20	2.28	2.22	0.9 vs 2.70
$10^5$	4.45	4.55	4.48	0.67 vs 1.56
$10^6$	8.72	8.82	8.69	0.35 vs 1.50
$10^7$	16.22	16.26	16.24	-0.12 vs 0.12

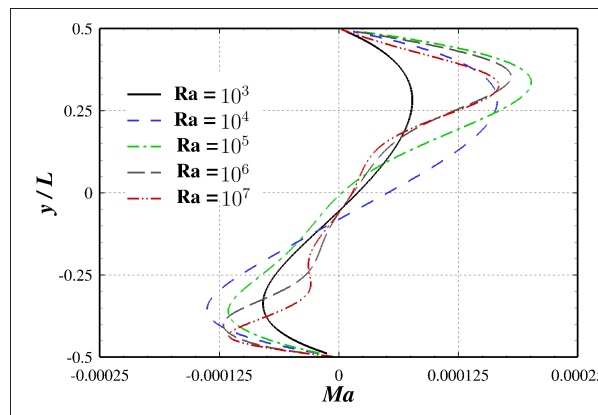
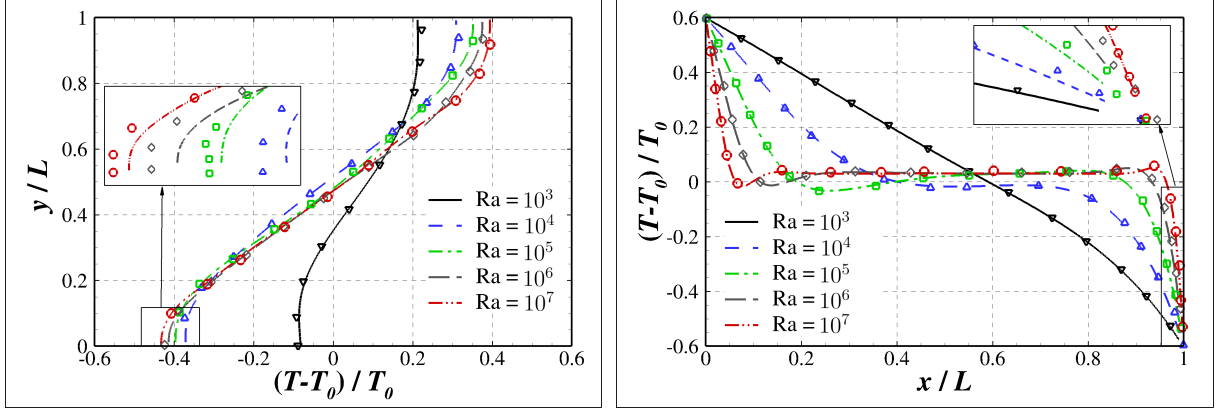


FIG. 7. Profiles of Mach number (normalized by speed of sound at  $T_0 = 600K$ ) at  $x/L = 0.5$  with the cavity inclined at  $15^\circ$ .

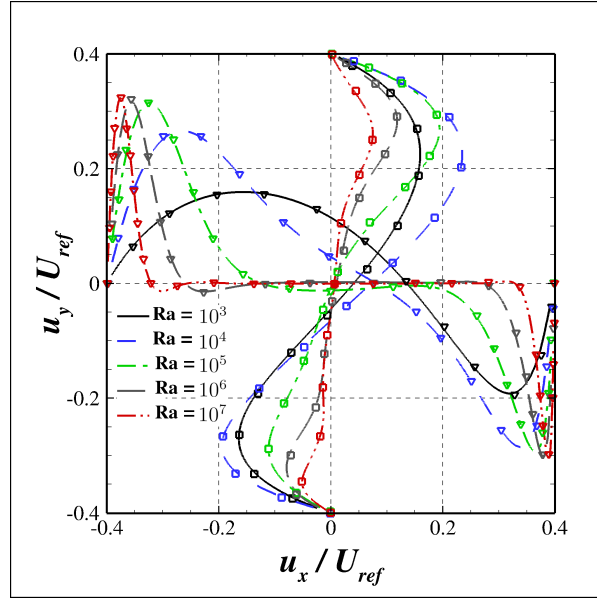
## 347 VI. CONCLUSIONS

348 In this paper, we extend the recently developed Farag’s pressure-based LB method implemented  
 349 in the commercial software ProLB, which has exhibited outstanding capability for supersonic flow,  
 350 to heat-dominated flow at low  $Ma$  with large temperature difference considering both aligned and  
 351 inclined boundaries. As demonstrated in ProLB, Farag’s pressure-based LB method prefers an  
 352 efficient hybrid strategy that solves the energy equation in a conventional FD manner, and directly  
 353 includes the conventionally solved temperature in the zeroth order moment of the distribution  
 354 functions to restore the energy equation. To address the thermal-coupled mass conservation chal-  
 355 lenge, we theoretically quantify the mass leakage (ML) at the boundary nodes within Farag’s LB  
 356 framework, and implemented a local mass correction in the solver based on that.



(a) Temperature profiles at  $x/L = 0.5$

(b) Temperature profiles at  $y/L = 0.5$



(c) Velocity profiles

FIG. 8. Profiles of temperature ((a)-(b)) and velocity (c) inclined cavity for different Rayleigh number, markers represent reference data<sup>11</sup>.

357 The canonical natural thermal convection in a square cavity heated by a large temperature  
 358 difference  $\Delta T/T_{ref} = 1.2$  is considered to assess the performance of the mass corrected pressure-  
 359 based LB method with the Rayleigh number ranging from  $10^3$  to  $10^7$  and the cavity inclined at  
 360 different angles. The numerical results show that the mass leakage is a serious challenge leading  
 361 to simulation crashes. Although the problem could be significantly relieved by applying aligned  
 362 boundaries with very fine grid resolutions, the reliability of simulations is still supposed to be ru-  
 363 ined when more time step is simulated. Fortunately, the proposed theoretical ML identification is  
 364 accurate, based on which the applied local mass correction is able to remove it cleanly. Together

365 with the mass correction, the high-speed featured Farag’s LB method implemented in ProLB per-  
 366 forms well over the considered  $10^3 \leq Ra \leq 10^7$  for both aligned and inclined boundaries.

367 The presented capability extension of Farag’s pressure-based LB method is limited to low  $Ma$   
 368 regime. However, it clearly illustrates the way to apply the method for thermal problems with  
 369 complex geometry involved. Moreover, it also enables the solver to deal with practical problems  
 370 where both low and high  $Ma$  thermal physics emerges, e.g. a cooling fan might has low  $Ma$  area  
 371 near the fix hub but high  $Ma$  area around the blade tips. That probably will be our next research  
 372 topic.

### 373 ACKNOWLEDGEMENTS

374 This work was performed within ProLB solver. Centre de Calcul Intensif d’Aix-Marseille is  
 375 acknowledged for granting access to its high performance computing resources. We also acknowl-  
 376 edge the supports of ANR, Renault, Airbus and SafranTech by the Industrial Chair Program AL-  
 377 BUMS (ANR-CHIND-18-ALBUMS). Deeply grateful to Song ZHAO for the inspiring discussion  
 378 about the mass conservation and heat transfer problems.

### 379 Appendix A: The discrete velocity model D3Q19

380 The discrete velocities ( $c_i$ ) as well as the corresponding weight factors ( $\omega_i$ ) of the applied  
 381 D3Q19 model are detailed in Table. III:

TABLE III. Discrete velocities and corresponding weights of D3Q19. The sub-index  $\alpha$  in  $c_{i\alpha}$  refers to the coordinates  $x$ ,  $y$ , and  $z$ .

		<b>D3Q19</b>	
$c_{i\alpha}$	$\omega_i$	(0,0,0)	1/3
		( $\pm 1,0,0$ )	1/18
		( $\pm 1,\pm 1,0$ )	1/36

382 Noticeably, to reduce the defect of rotation invariant using D3Q19, a set of Hermite basis with  
 383 improved orthogonality is adopted in the recursive regularization of the distribution functions. The


384 improved Hermite basis is formulated as

$$385 \quad \mathcal{H}_{i,(\alpha\beta\gamma)\subset(x,y,z)}^{(3)} = \begin{pmatrix} \text{cyc}(H_{i,xxxy}^{(3)} + H_{i,yzzz}^{(3)}) \\ \text{cyc}(H_{i,xzzz}^{(3)} + H_{i,xyyy}^{(3)}) \\ \text{cyc}(H_{i,yyyz}^{(3)} + H_{i,xxxz}^{(3)}) \\ H_{i,xxxy}^{(3)} - H_{i,yzzz}^{(3)} \\ H_{i,xzzz}^{(3)} - H_{i,xyyy}^{(3)} \\ H_{i,yyyz}^{(3)} - H_{i,xxxz}^{(3)} \end{pmatrix} \quad (A1)$$

386 where  $(\alpha\beta\gamma) \subset (x,y,z)$ , and  $H_{i,\alpha\beta\gamma}$  is the original 3rd order Hermite basis tensor

$$387 \quad H_{i,\alpha\beta\gamma}^{(3)} = c_{i,\alpha}c_{i,\beta}c_{i,\gamma} - c_s^2[c_i\delta]_{\alpha\beta\gamma} \quad (A2)$$


## 388 Appendix B: Governing equations and the hybrid solving process

By combining Farag's pressure-based LB method  finite-difference method, the commercial software ProLB solves the full compressible Navier-Stokes equations, i.e.,

$$\frac{\partial \rho}{\partial t} + \frac{\partial \rho u_\alpha}{\partial x_\alpha} = 0 \quad (B1a)$$

$$\frac{\partial \rho u_\alpha}{\partial t} + \frac{\partial \rho u_\alpha u_\beta}{\partial x_\beta} = -\frac{\partial p}{\partial x_\alpha} + \frac{\partial}{\partial x_\beta} \left[ \mu \left( \frac{\partial u_\alpha}{\partial x_\beta} + \frac{\partial u_\beta}{\partial x_\alpha} - \frac{2}{3} \frac{\partial u_\gamma}{\partial x_\gamma} \delta_{\alpha\beta} \right) \right] + F_\alpha \quad (B1b)$$

$$\frac{\partial s}{\partial t} + \mathbf{u} \frac{\partial s}{\partial x_\alpha} = \frac{1}{\rho T} \left[ \mu \left( \frac{\partial u_\alpha}{\partial x_\beta} + \frac{\partial u_\beta}{\partial x_\alpha} - \frac{2}{3} \frac{\partial u_\gamma}{\partial x_\gamma} \delta_{\alpha\beta} \right) \frac{\partial u_\alpha}{\partial x_\beta} + \frac{\partial}{\partial x_\alpha} \left( \lambda \frac{\partial T}{\partial x_\alpha} \right) \right] \quad (B1c)$$

389 where  $F_\alpha$  is  external force, e.g., the gravity used in this study, and  $s$  is the entropy.

390 The solving process is illustrated in Fig. 9. Clearly, the LB process in the left-hand side solves  
 391 the mass and momentum equations (the first two in Eq. (B1)), while the FD process in the right-  
 392 hand side solves the energy equation. The two processes are deeply coupled: the LB process relies  
 393 on the thermal variable  $\theta = T/T_0$  solved by the FD process to include thermal and compressible  
 394 effects, and, in turn, the FD process uses  $\rho$  and  $\mathbf{u}$  solved by the LB process to complete the heat  
 395 convection. The FD process will be detailed in the followed Appendix C.  
 396

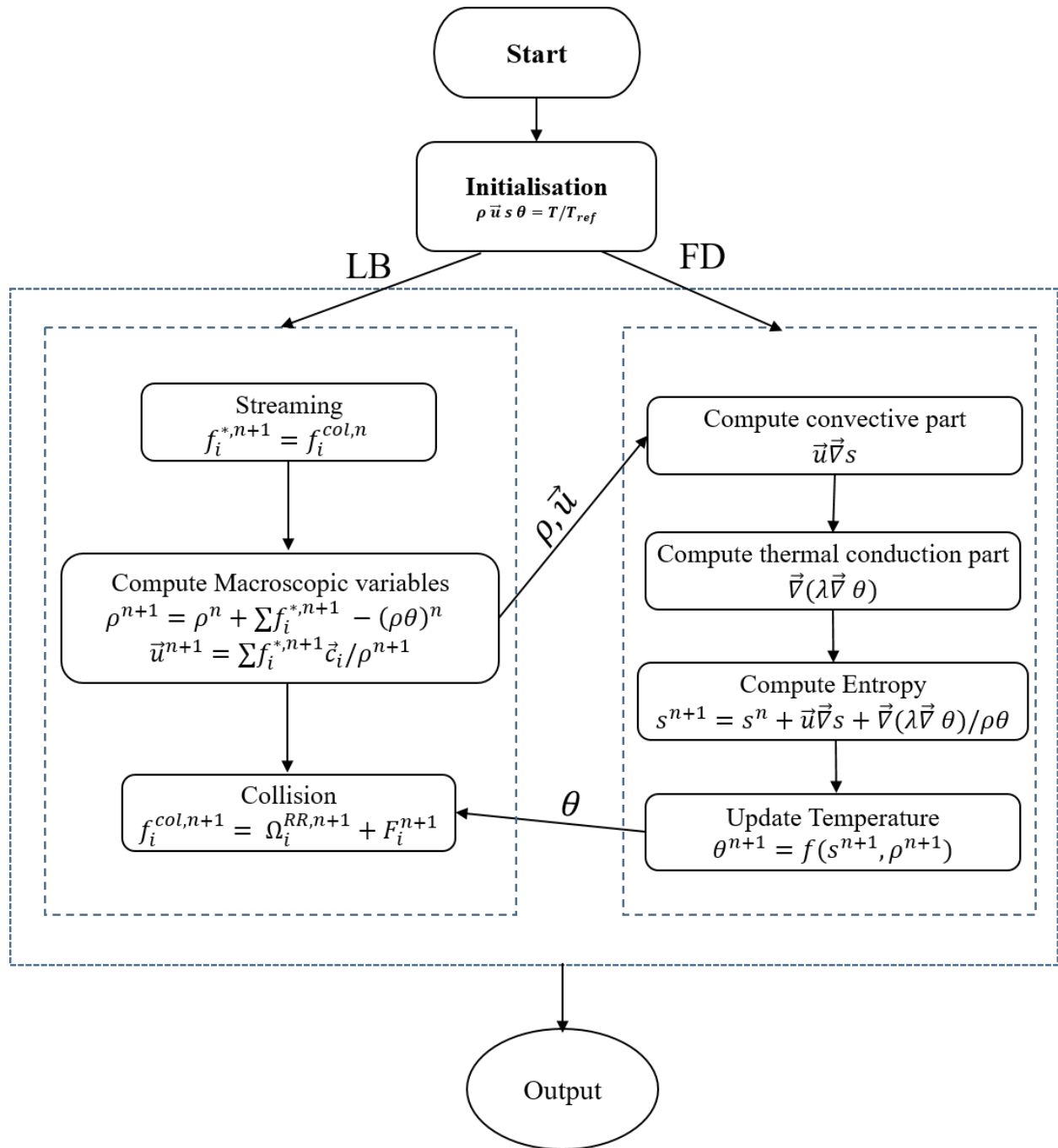


FIG. 9. Sketch of the hybrid strategy adopted in ProLB

## 397 Appendix C: Numerical schemes for the energy equation

398 The energy equation in Eq. (B1) is solved using a FD method taking the entropy as the di-  
 399 rect thermal variable. The temporal derivative and convective term in the left-hand side are  
 400 discretized using the first-order explicit Euler scheme and the second-order Monotonic Upwind  
 401 Scheme for Conservation Laws (MUSCL-Hancock)<sup>37</sup>, respectively. The viscous heat dissipation  
 402 and Fourier heat transfer terms on right-hand side are discretized using second order central dif-  
 403 ference schemes.

### 404 1. Discretization of terms on the left-hand side

405 The terms on the left-hand side of Eq. (B1c) are discretized as

$$406 \quad \frac{s_i^{n+1} - s_i^n}{\Delta t} + \frac{F(s_{i+\frac{1}{2}}^n) - F(s_{i-\frac{1}{2}}^n)}{\Delta x} \quad (C1)$$

407 where  $n$ ,  $i$  and  $i \pm \frac{1}{2}$  represent respectively the time step, cell identity and boundary of the  $i^{\text{th}}$  cell.

408 The convective flux  $F(s_{i+\frac{1}{2}}^n)$  and  $F(s_{i-\frac{1}{2}}^n)$  are computed through the following three steps:

1. Data reconstruction. The inter-cell values at the left and right sides of the  $i^{\text{th}}$  cell is firstly  
 evaluated by extrapolation, i.e.,

$$s_{i,L} = s_i - \frac{1}{2} \Delta_i \quad (C2a)$$

$$s_{i,R} = s_i + \frac{1}{2} \Delta_i \quad (C2b)$$

409 where the  $\Delta_i$  is a high order approximation of the slop at the center of  $i^{\text{th}}$  cell which is  
 410 calculated by

$$411 \quad \Delta_i = \frac{1}{2} \left[ (1 + \Phi)(s_i - s_{i-1}) + (1 - \Phi)(s_{i+1} - s_i) \right] \quad (C3)$$

412 with  $\Phi = \frac{1}{3} \left[ \frac{2\Delta t u_i}{\Delta x} - \text{sign}(u_i) \right]$  proposed by Toro<sup>37</sup>.

2. Data evolution. The boundary values of the cell is further evolved by a semi-time step  $\frac{\Delta t}{2}$ ,  
 i.e.,

$$\bar{s}_{i,L} = s_{i,L} + \frac{2\Delta t u_i}{\Delta x} (s_{i,L} - s_{i,R}) \quad (C4a)$$

$$\bar{s}_{i,R} = s_{i,R} + \frac{2\Delta t u_i}{\Delta x} (s_{i,L} - s_{i,R}) \quad (C4b)$$

3. Piece-wise construction of convective flux. The convective flux  $F(s_{i+\frac{1}{2}})$  and  $F(s_{i-\frac{1}{2}}^n)$  are then evaluated by

$$F(s_{i+\frac{1}{2}}) = \begin{cases} u_i \bar{s}_{i,R} & \text{if } u_i \geq 0 \\ u_i \bar{s}_{i+1,L} & \text{if } u_i \leq 0 \end{cases} \quad (\text{C5a})$$

$$F(s_{i-\frac{1}{2}}) = \begin{cases} u_i \bar{s}_{i-1,R} & \text{if } u_i \geq 0 \\ u_i \bar{s}_{i,L} & \text{if } u_i \leq 0 \end{cases} \quad (\text{C5b})$$

## 413 2. Discretization of terms on the right-hand side

The Fourier part  $\frac{\partial}{\partial x_\alpha} \left( \lambda \frac{\partial T}{\partial x_\alpha} \right)$  and the viscous heat dissipation  $\left( \frac{\partial u_\alpha}{\partial x_\beta} + \frac{\partial u_\beta}{\partial x_\alpha} - \frac{2}{3} \frac{\partial u_\gamma}{\partial x_\gamma} \delta_{\alpha\beta} \right) \frac{\partial u_\alpha}{\partial x_\beta}$  are discretized here. Since  $\lambda$  in the Fourier part varies with  $T$ , the term is decomposed into two parts:  $\frac{\partial \lambda}{\partial x_\alpha} \frac{\partial T}{\partial x_\alpha}$  and  $\lambda \frac{\partial^2 T}{\partial x_\alpha^2}$ . Apparently, the first-order spatial derivatives of  $\mathbf{u}$ ,  $\lambda$  and  $T$  as well as the second-order spatial derivatives of  $T$  are required to be discretized. In ProLB, all of them are discretized using second-order accurate center difference schemes, i.e.,

$$\frac{\partial \phi}{\partial x_\alpha} = \frac{\phi_{i+1} - \phi_{i-1}}{2\Delta x_\alpha} \quad (\text{C6a})$$

$$\frac{\partial T^2}{\partial x_\alpha^2} = \frac{T_{i+1} - 2T_i + T_{i-1}}{\Delta x_\alpha^2} \quad (\text{C6b})$$

414 where  $\phi = \mathbf{u}$ ,  $\lambda$  and  $T$ , and  $\alpha \in [x, y, z]$ .

## 415 Appendix D: A cut-cell immersed boundary treatment

416 A cut-cell immersed based recursive regularized boundary treatment is adopted in ProLB to  
 417 reconstruct the LB distribution functions and the temperature. In the method, the macroscopic  
 418 variables (e.g.,  $p$ ,  $\mathbf{u}$  and  $T$ ) are reconstructed through interpolation, based on which  $\rho = p/(RT)$   
 419 and the equilibrium parts of the distribution functions are directly calculated using Eq. (2). Mean-  
 420 while, the off-equilibrium parts are reconstructed from the spatial derivatives of macroscopic vari-  
 421 ables according to the recursive regularization analysis<sup>38</sup> with the required spatial derivatives are  
 422 calculated using the finite difference method (centered or not) using values of the previous time  
 423 step. As an introduction of the immersed boundary method, the following is focused on the details  
 424 of the reconstruction of the macroscopic variables.

425 The interpolation of macroscopic variables is illustrated in Fig. 10. As shown in Fig. 10,  
 426 two reference points (i.e., Ref<sub>1</sub> and Ref<sub>2</sub> one and two grid spacing away from the boundary node,

427 respectively) in the fluid domain along the local normal direction of the wall are introduced to assist  
 428 the interpolation. With the variables at the reference points interpolated from the surrounding fluid  
 429 nodes, values at the concerned boundary node are interpolated from the reference points according  
 430 to specific boundary conditions.

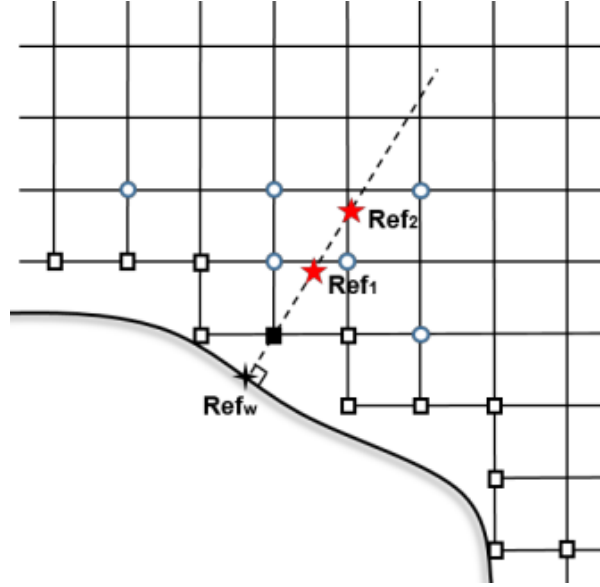


FIG. 10. Sketch of interpolation-based immersed boundary method. The black square and blue circles represent a boundary node and its neighbor nodes, respectively.

431  
432

433 Firstly, the macroscopic variables at the reference points are computed through an inverse distance  
 434 weighting (IDW) method, i.e.,

$$435 \quad \phi_{x_{ref}} = \sum_{i=1}^N \frac{d(x_i, x_{ref})^{-p}}{\sum_{i=1}^N d(x_i, x_{ref})^{-p}} \phi_{x_i} \quad (D1)$$

436 where  $\phi$  represents the required macroscopic variables (e.g.,  $\rho$ ,  $\mathbf{u}$  and  $T$ ),  $d(x_i, x_{ref})$  the distance  
 437 of the  $i^{th}$  neighbor point to the reference point, and the coefficient  $P = 2$  is preferred here<sup>39,40</sup>.

Then, the macroscopic variables at the concerned boundary node is interpolated from those at the reference points to implement different kinds of boundary condition. In this paper, two kinds of boundary condition, the Dirichlet and Neumann boundary conditions, are implemented. For Dirichlet boundary conditions, e.g., the velocity of static walls and  $T$  at isothermal walls, the projection point (see  $Ref_w$  in Fig. 10) of the concerned boundary node at the wall is included in the interpolation stencil. The interpolation can be formulated as

$$\phi_{BN} = \frac{2\Delta x^2}{(\Delta_w + \Delta x)(\Delta_w + 2\Delta x)} \phi_w + \frac{2\Delta_w}{\Delta_w + \Delta x} \phi_1 - \frac{\Delta_w}{\Delta_w + 2\Delta x} \phi_2 \quad (D2a)$$



where  $\phi_{BN}$  is the required variables at the boundary node,  $\phi_w$  is those at the projection point,  $\phi_1$  and  $\phi_2$  are those at Ref<sub>1</sub> and Ref<sub>2</sub>, respectively, and  $\delta_w$  and  $\delta_x$  represent the wall distance of boundary node and the local grid spacing, respectively. For the Neumann boundary condition, such as  $\frac{\partial p}{\partial n} = 0$  and the adiabatic wall ( $\frac{\partial T}{\partial n} = 0$ ), the second order Lagrangian interpolation is used to reconstruct the required variables as

$$\phi_{BN} = \frac{4(\Delta x + \Delta_w)\phi_1 - (\Delta x + 2\Delta_w)\phi_2}{2\Delta_w + 3\Delta x} \quad (D3a)$$

438 **REFERENCES**

- 439 <sup>1</sup>S. M. Ghiaasiaan, *Convective heat and mass transfer* (CRC Press, 2018).
- 440 <sup>2</sup>T. Cebeci and P. Bradshaw, *Physical and computational aspects of convective heat transfer*  
441 (Springer Science & Business Media, 2012).
- 442 <sup>3</sup>J. Salat, S. Xin, P. Joubert, A. Sergent, F. Penot, and P. Le Quere, “Experimental and numerical  
443 investigation of turbulent natural convection in a large air-filled cavity,” *International Journal of*  
444 *Heat and Fluid Flow* **25**, 824–832 (2004).
- 445 <sup>4</sup>S. Mergui and F. Penot, “Convection naturelle en cavité carrée différentiellement chauffée: in-  
446 vestigation expérimentale à  $Ra= 1, 69 \times 10^9$ ,” *International Journal of Heat and Mass Transfer*  
447 **39**, 563–574 (1996).
- 448 <sup>5</sup>G. de Vahl Davis, “Natural convection of air in a square cavity: a bench mark numerical solu-  
449 tion,” *International Journal for Numerical Methods in Fluids* **3**, 249–264 (1983).
- 450 <sup>6</sup>D. Chenoweth and S. Paolucci, “Natural convection in an enclosed vertical air layer with large  
451 horizontal temperature differences,” *Journal of Fluid Mechanics* **169**, 173–210 (1986).
- 452 <sup>7</sup>P. Le Quéré, “Accurate solutions to the square thermally driven cavity at high Rayleigh number,”  
453 *Computers & Fluids* **20**, 29–41 (1991).
- 454 <sup>8</sup>N. Massarotti, P. Nithiarasu, and O. Zienkiewicz, “Characteristic-based-split (CBS) algorithm  
455 for incompressible flow problems with heat transfer,” *International Journal of Numerical Meth-*  
456 *ods for Heat & Fluid Flow* (1998).
- 457 <sup>9</sup>C. Wan, B. Patnaik, G. Wei, and D, “A new benchmark quality solution for the buoyancy-  
458 driven cavity by discrete singular convolution,” *Numerical Heat Transfer: Part B: Fundamentals*  
459 **40**, 199–228 (2001).
- 460 <sup>10</sup>J. Vierendeels, B. Merci, and E. Dick, “Numerical study of natural convective heat transfer with  
461 large temperature differences,” *International Journal of Numerical Methods for Heat & Fluid*  
462 *Flow* (2001).
- 463 <sup>11</sup>J. Vierendeels, B. Merci, and E. Dick, “Benchmark solutions for the natural convective heat  
464 transfer problem in a square cavity with large horizontal temperature differences,” *International*  
465 *Journal of Numerical Methods for Heat & Fluid Flow* (2003).
- 466 <sup>12</sup>C. Cintolesi, A. Petronio, and V. Armenio, “Large eddy simulation of turbulent buoyant flow in  
467 a confined cavity with conjugate heat transfer,” *Physics of Fluids* **27**, 095109 (2015).
- 468 <sup>13</sup>Y. Feng, P. Sagaut, and W. Tao, “A three dimensional lattice model for thermal compressible

- 469 flow on standard lattices,” *Journal of Computational Physics* **303**, 514–529 (2015).
- 470 <sup>14</sup>G. Farag, S. Zhao, T. Coratger, P. Boivin, G. Chiavassa, and P. Sagaut, “A pressure-based reg-  
471 ularized lattice-Boltzmann method for the simulation of compressible flows,” *Physics of Fluids*  
472 **32**, 066106 (2020).
- 473 <sup>15</sup>T. Krüger, H. Kusumaatmaja, A. Kuzmin, O. Shardt, G. Silva, and E. M. Viggien, “The lattice  
474 Boltzmann method,” Springer International Publishing **10**, 978–3 (2017).
- 475 <sup>16</sup>O. Filippova and D. Hänel, “Lattice-BGK model for low Mach number combustion,” *Internation-  
476 al Journal of Modern Physics C* **9**, 1439–1445 (1998).
- 477 <sup>17</sup>O. Filippova and D. Hänel, “A novel lattice BGK approach for low Mach number combustion,”  
478 *Journal of Computational Physics* **158**, 139–160 (2000).
- 479 <sup>18</sup>K. Yamamoto, X. He, and G. D. Doolen, “Simulation of combustion field with lattice Boltzmann  
480 method,” *Journal of statistical physics* **107**, 367–383 (2002).
- 481 <sup>19</sup>S. A. Hosseini, H. Safari, N. Darabiha, D. Thévenin, and M. Krafczyk, “Hybrid lattice  
482 Boltzmann-finite difference model for low Mach number combustion simulation,” *Combustion  
483 and Flame* **209**, 394–404 (2019).
- 484 <sup>20</sup>S. Hosseini, A. Abdelsamie, N. Darabiha, and D. Thévenin, “Low-Mach hybrid lattice  
485 Boltzmann-finite difference solver for combustion in complex flows,” *Physics of Fluids* **32**,  
486 077105 (2020).
- 487 <sup>21</sup>Y. Cao, “Variable property-based lattice Boltzmann flux solver for thermal flows in the low Mach  
488 number limit,” *International Journal of Heat and Mass Transfer* **103**, 254–264 (2016).
- 489 <sup>22</sup>O. Filippova and D. Hänel, “Grid refinement for lattice-BGK models,” *Journal of Computational  
490 Physics* **147**, 219–228 (1998).
- 491 <sup>23</sup>T. Lee, C.-L. Lin, and L.-D. Chen, “A lattice Boltzmann algorithm for calculation of the laminar  
492 jet diffusion flame,” *Journal of Computational Physics* **215**, 133–152 (2006).
- 493 <sup>24</sup>G. Farag, T. Coratger, G. Wissocq, S. Zhao, P. Boivin, and P. Sagaut, “A unified hybrid Lattice-  
494 Boltzmann method for compressible flows: -Bridging between pressure-based and density-based  
495 methods,” *Physics of Fluids* **33**, 086101 (2021).
- 496 <sup>25</sup>F. J. Alexander, H. Chen, S. Chen, and G. Doolen, “Lattice Boltzmann model for compressible  
497 fluids,” *Physical Review A* **46**, 1967 (1992).
- 498 <sup>26</sup>Y. Qian, “Simulating thermohydrodynamics with lattice BGK models,” *Journal of Scientific  
499 Computing* **8**, 231–242 (1993).
- 500 <sup>27</sup>R. Qiu, R. Chen, C. Zhu, and Y. You, “A hermite-based lattice Boltzmann model with artifi-

501 cial viscosity for compressible viscous flows,” *International Journal of Modern Physics B* **32**,  
502 1850157 (2018).

503 <sup>28</sup>X. Yin and J. Zhang, “Mass conservation across moving solid-fluid boundaries in lattice Boltz-  
504 mann method,” in *The 20th Annual Conference of the CFD Society of Canada*, pp. 9–11.

505 <sup>29</sup>J. Bao, P. Yuan, and L. Schaefer, “A mass conserving boundary condition for the lattice Boltz-  
506 mann equation method,” *Journal of Computational Physics* **227**, 8472–8487 (2008).

507 <sup>30</sup>H. Yu, X. Chen, Z. Wang, D. Deep, E. Lima, Y. Zhao, and S. D. Teague, “Mass-conserved volu-  
508 metric lattice Boltzmann method for complex flows with willfully moving boundaries,” *Physical*  
509 *Review E* **89**, 063304 (2014).

510 <sup>31</sup>L. XU, E. SERRE, and P. SAGAUT, “A theoretical analysis of mass leakage at boundaries  
511 within the lattice Boltzmann method,” *Journal of Computational Physics*, Under Review (2021).

512 <sup>32</sup>Z. Guo, C. Zheng, and B. Shi, “Discrete lattice effects on the forcing term in the lattice Boltz-  
513 mann method,” *Physical Review E* **65**, 046308 (2002).

514 <sup>33</sup>S. Chapman and T. Cowling, “The mathematical theory of non-uniform gases, cambridge univ,”  
515 Press, Cambridge, England (1970).

516 <sup>34</sup>C. Coreixas, G. Wissocq, G. Puigt, J.-F. Boussuge, and P. Sagaut, “Recursive regularization step  
517 for high-order lattice Boltzmann methods,” *Physical Review E* **96**, 033306 (2017).

518 <sup>35</sup>Y.-L. Feng, S.-L. Guo, W.-Q. Tao, and P. Sagaut, “Regularized thermal lattice Boltzmann  
519 method for natural convection with large temperature differences,” *International Journal of Heat*  
520 *and Mass Transfer* **125**, 1379–1391 (2018).

521 <sup>36</sup>Y. Feng, S. Guo, J. Jacob, and P. Sagaut, “Solid wall and open boundary conditions in hybrid  
522 recursive regularized lattice Boltzmann method for compressible flows,” *Physics of Fluids* **31**,  
523 126103 (2019).

524 <sup>37</sup>E. F. Toro, *Riemann solvers and numerical methods for fluid dynamics: a practical introduction*  
525 (Springer Science & Business Media, 2013).

526 <sup>38</sup>G. Farag, S. Zhao, G. Chiavassa, and P. Boivin, “Consistency study of Lattice-Boltzmann  
527 schemes macroscopic limit,” *Physics of Fluids* **33**, 037101 (2021).

528 <sup>39</sup>T. Gao, Y.-H. Tseng, and X.-Y. Lu, “An improved hybrid Cartesian/immersed boundary method  
529 for fluid–solid flows,” *International Journal for Numerical Methods in Fluids* **55**, 1189–1211  
530 (2007).

531 <sup>40</sup>R. Franke, “Scattered data interpolation: tests of some methods,” *Mathematics of computation*  
532 **38**, 181–200 (1982).